Actuation of a Lean-Premixed Flame by Diffuse Non-Equilibrium Nanosecond-Pulsed Plasma at Atmospheric Pressure

M.D.G. Evans,[1,2,a)] J.M. Bergthorson,[2] and S. Coulombe[1]

[1]*Plasma Processing Laboratory, Department of Chemical Engineering, McGill University, Montréal, H3A 0C5, Canada*

[2]*Alternative Fuels Laboratory, Department of Mechanical Engineering, McGill University, Montréal, H3A 0C3, Canada*

This study investigates the effect of diffuse non-equilibrium nanosecond-pulsed plasma at atmospheric pressure on a lean-premixed CH_4-air flame ($\phi = 0.65$, $P \sim 0.3$ kW). The domain of diffuse plasma existence is explored for both the case of the cold flow (no flame) and for the case where a flame is stabilized downstream. The dynamics of plasma propagation and the flame displacement, following a high-voltage pulse, were measured using ICCD imaging. The energy of the plasma was measured using electrical probes and measurements of the second positive system of nitrogen were used to determine the rotational temperature and vibrational populations in the plasma. The effect of plasma on a flame was investigated by varying the pulse repetition frequency gradually from 1 to 7 kHz. Time-resolved imaging of the plasma emission shows that the primary streamer travels at higher velocities with increased pulsing frequency and with the presence of a flame ignited downstream of the discharge. Time-resolved imaging of the flame, following a high-voltage pulse, shows that the flame moves upstream into the unburned methane-air mixture with increased pulsing frequency. As the flame is displaced upstream, the nature of the discharge also changes, whereby less energy is coupled to the gas volume. Spectroscopic results reveal that the region in which the flame stabilizes is that of highest vibrational excitation and lowest rotational temperature. This actuation method is evidence of low-temperature chemical flame enhancement and potential control of a lean-premixed laminar flame at atmospheric pressure.

I. INTRODUCTION

Plasma-assisted combustion (PAC) and plasma-assisted ignition (PAI) by non-equilibrium plasma are of growing interest to the scientific community for the thermal, chemical, and hydrodynamic benefits provided to the combustion process.[1,2,3] The use of low-temperature radical pools to enhance and accelerate burning rates was computationally predicted almost thirty years ago,[4] and since then PAI and PAC have been the focus of many research groups around the world. PAI has been shown to reduce the ignition delay time, and facilitate utilization of combustible mixtures.[5,6,7] Research on PAC has primarily focused on low-pressure environments, for the aerospace industry, to enhance the burning rate of flames[8] and provide flame anchoring.[9] Atmospheric pressure PAC has mainly focused on the thermal enhancement of combustion through the use of nanosecond-duration spark discharges.[10] These produce high number densities of reactive species, and ultrafast heating of the bulk gas.[11,12] Although nanosecond-duration sparks have been used to stabilize turbulent flames,[13] and extend the lean-burn regime,[14] they also increase the output of pollutants such as NO in gas-turbine engines.[15] Thus, efforts in atmospheric pressure PAC for the gas-turbine industry should be placed on the use of low-temperature high-energy radical pools to provide a more complete and low-emission combustion process.

[a)] Author to whom correspondence should be addressed - Electronic mail: mathew.evans@mail.mcgill.ca

Numerical work has shown that replacing minute quantities of the O_2 in a CH_4-air mixture with $O_2(a^1\Delta_g)$ molecules, at atmospheric pressure, significantly increases the flame speed.[16] This is due to the enhancement of low-temperature chain-branching reactions in the flame front, which produce increased quantities of CH_3, CH_2O, OH, O, and H. This increase has been experimentally confirmed by injecting O_3 or $O_2(a^1\Delta_g)$ molecules, far upstream of the burner's inlet for CH_4-O_2 diffusion flames.[17,18] Although the addition of $O_2(a^1\Delta_g)$ particles will slightly increase the concentration of NO in an engine's exhaust,[19] the increase in the flame speed will extend the lean-burn limit. This increase in the flame speed allows a leaner flame to burn with far less NO produced in its exhaust, when compared to an un-activated flame with identical flame speed.

In fuel-lean CH_4-air low-temperature plasma, the production of $O_2(a^1\Delta_g)$ and $O(^1D)$ takes place following collisions between ground-state O_2 and excited neutrals of N_2 ($C^3\Pi_u$, $B^3\Pi_g$, $a^1\Pi_g$…).[20] These electronic states of N_2 are produced by electron impact in the discharge at moderate reduced electric fields (E/N), and transmit their energy through collisions to produce $O(^1D)$ and $O_2(a^1\Delta_g)$ particles. Additionally, collisional quenching rates of $N_2(C^3\Pi_u, B^3\Pi_g, a^1\Pi_g…)$ by neutral CH_4 are quite high, and can lead to the dissociation of fuel molecules, producing active particles (H, CH_3, CH_2, CH…) that can further increase the flame speed.[20] Recent work has shown that a diffuse plasma with a significantly lower gas temperature (300-400 K) than a nanosecond-duration spark (1800-2200 K) can be used at atmospheric pressure to activate fuel streams,[21] increase the blow off velocity of premixed CH_4-air flames,[22] and suppress thermo-acoustic instabilities.[23,24]

This study pertains to the actuation of a stabilized, lean-premixed CH_4-air flame by diffuse non-equilibrium nanosecond-pulsed plasma at atmospheric pressure. In an effort to simultaneously deliver the highest number density of chemically active low-temperature species and provide instantaneous actuation of the flame, the plasma volume is directly coupled to the flame front. Two flow conditions are studied: the first is that of the diffuse plasma in the non-ignited CH_4-air mixture (denoted as cold flow), and the second is that of the discharge with a stagnation flame stabilized downstream (denoted downstream flame). The domain of the diffuse plasma is explored (extinction-to-spark), for both flows by varying the pulse-repetition frequency of the discharge. Electrical diagnostics are presented and the energy per pulse is reported. Time-resolved ICCD imaging of the plasma emission is used to explain the upper frequency limit of the diffuse plasma for both flow conditions. Spatially-resolved spectroscopic measurements are presented and the rotational temperature and vibrational population of the $N_2(C^3\Pi_u)$ state are determined. The measurements allow for a more detailed understanding on the location of the flame stabilization. Finally, the displacement and relaxation of the flame following a high-voltage pulse is reported using time-resolved ICCD imaging.

II. EXPERIMENTAL

A. Burner Assembly & Gas Discharge Configuration

Figure 1 shows the burner assembly and the gas discharge configuration. A mixture of CH_4 and air ($\phi = 0.65$, $u = 0.65$ m/s) flows through the inner nozzle (20 mm I.D.), while a co-flow stream of N_2 flows in the outer nozzle (45 mm I.D.) to isolate the flame from the laboratory's surroundings. Here, u is the average velocity at the exit of the nozzle and ϕ is the equivalence ratio of the CH_4-air mixture, given by (1).

$$\phi = \frac{\left(\dot{n}_{\mathrm{CH_4}} / \dot{n}_{\mathrm{air}}\right)}{\left(\dot{n}_{\mathrm{CH_4}} / \dot{n}_{\mathrm{air}}\right)_{\mathrm{st}}} \tag{1}$$

In (1), $\dot{n}_{CH_4}$ and $\dot{n}_{air}$ are the molar flow rates of CH_4 and air respectively, and $\left(\dot{n}_{\mathrm{CH_4}} / \dot{n}_{\mathrm{air}}\right)_{\mathrm{st}}$ is the stoichiometric ratio needed for complete combustion. A water-cooled stainless-steel stagnation plate is placed 40 mm downstream from the nozzle exit, with a coolant flow rate of 45 LPM. The stagnation plate was electrically insulated to prevent it from acting as a ground in the electrical circuit. The gas discharge configuration consists of a pair of stainless steel pins (1.3 mm in diameter), located 15 mm above the exit of the nozzle. These pins are powered by a high-voltage nanosecond pulse generator[22] connected to the anode while the cathode is connected to ground. The inter-electrode distance is 11 mm. The electrode tips were sharpened to locally increase the electric field, and the radius of curvature is approximately 250 μm. The capacitance of the cables and electrodes is 13.6 pF. The set of brass nozzles were sprayed with a dielectric varnish and electrically insulated, using 1/4" rubber supports, so as to eliminate the formation of plasma between the anode and the burner's surface. A stabilized flame ($P = 272$ W) could then be lit downstream of the plasma, depending on the explored flow condition (cold flow or downstream flame). The burner assembly allows for a stagnation flame to be located in the velocity field where the laminar flame speed equals that of the unburned CH_4-air mixture. Therefore, a change in the flame's position, in a spatially varying velocity field, may imply a change in the flame's speed and, therefore, its reactivity.

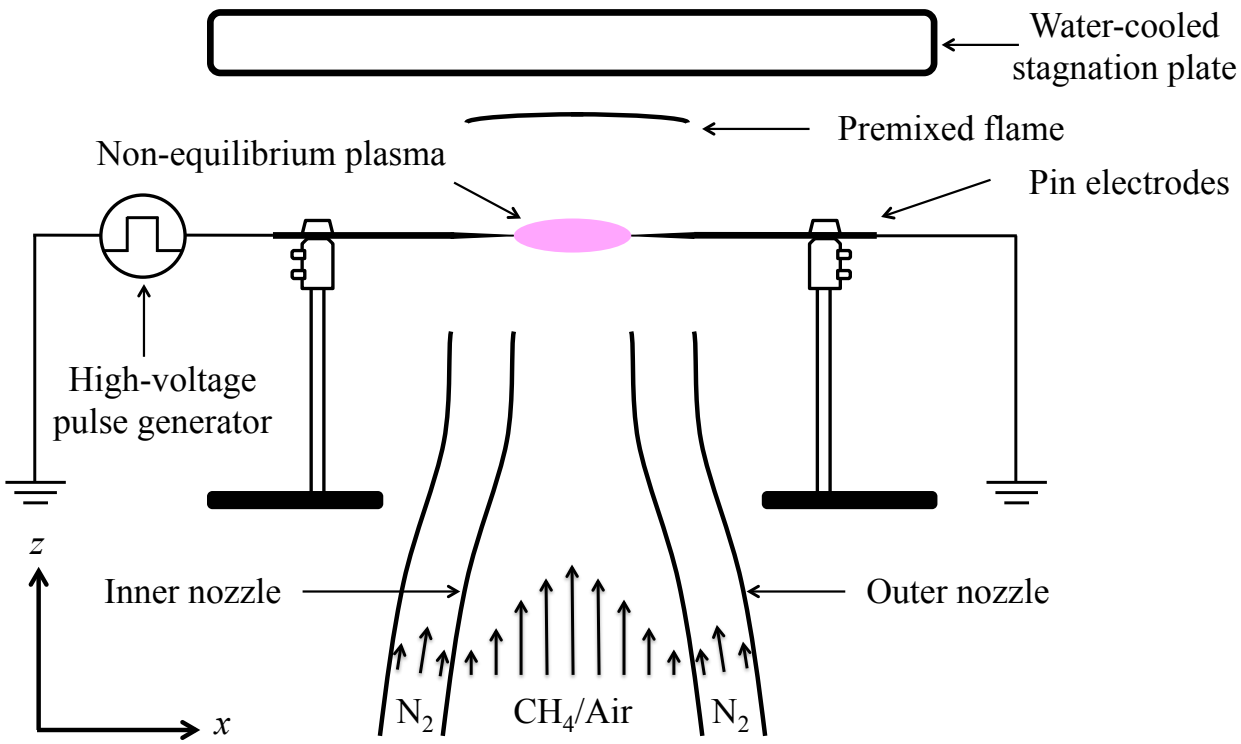

FIG. 1. Schematic of the stagnation-plate burner apparatus and the gas discharge configuration (side view of burner).

B. Electrical Diagnostics & Time-Resolved ICCD Imaging

Figure 2 shows a schematic of the apparatus used for time-resolved imaging and electrical diagnostics. The output of the pulse generator was measured and monitored with a high-voltage probe (*Tektronix*, P6015A, 3 pF, 100 MΩ). The discharge current was measured with a Rogowski coil (*Pearson Electronics*, Model 110A, 10 A/V). All electrical measurements were recorded with a digital oscilloscope (*Tektronix*, TDS-3054B), and synchronization of all the measurements was achieved using the trigger generator (*Berkley Nucleonics*, BNC 565). This trigger generator also acts as a master clock for the ICCD imaging scheme, where it activates the pulse generator, triggers the oscilloscope, and triggers the camera (*Cooke Corporation*, PCO, DiCAM-PRO). The camera is equipped with an aspherical lens assembly (*Tamron*, AF28-300mm XRDi), and the spatial resolution of the recorded images is 17.23 pixels/mm. Since the emission spectrum of the discharge is primarily composed of the second positive system of nitrogen (detailed in Section III.C), no additional optical filters were used. The computer controls the exposure, delay and number of accumulations of the ICCD camera. The camera gate is read out to the oscilloscope along with the voltage and current of the discharge. Each image is comprised of a series of on-CCD accumulations prior to being read out. The exposure time, t_{exp}, of the camera for imaging the plasma emission, and the flame, is 10 ns, and 1 µs, respectively. The number of on-CCD accumulations was 300.

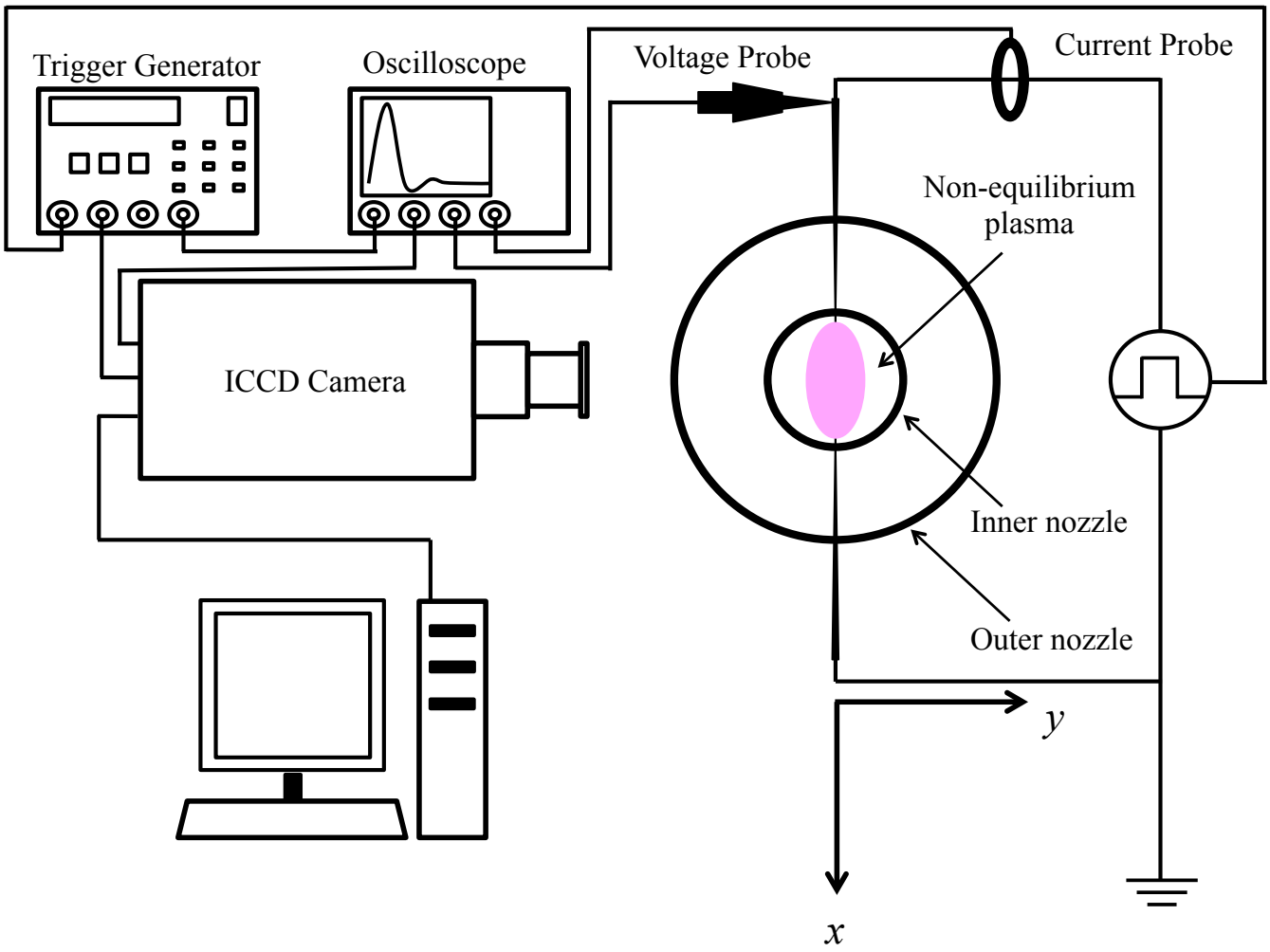

FIG. 2. Schematic of the apparatus used for electrical diagnostics and time-resolved ICCD imaging (top view of burner).

C. Optical Emission Spectroscopy

Figure 3 shows the experimental apparatus used for optical emission spectroscopy (OES). The light produced by the discharge is collected with a set of lenses and filters in order to properly collimate and collect the light prior to focusing on the spectrometer's entrance slit. First, the light passes through an iris, which reduces the solid angle of collection. Then it is collected by the first lens (f = 150 mm), passes through a high-pass filter ($\lambda > 280$ nm) and is collected by the second lens (f = 200 mm). The filter is placed between the two lenses in order to avoid second-order reflections that might occur from higher energy molecular bands present at lower wavelengths. The light is collected by an optical fiber (200 µm bundle) and sent to the spectrometer (*Acton*, SP2300i, f = 30 cm) equipped with a CCD camera (*Princeton Instruments*, PIXIS 256, 1024×256 pixels). The imaged spot size has a diameter of 150 µm, resulting in an overall 4/3 magnification factor. The spectral resolution achieved with this collection apparatus is $\Delta\lambda$ = 0.07 nm. The optics rail is mounted on a micrometric

displacement stage, allowing for displacement across the inter-electrode gap in the *x*-direction, from the tip of the anode to the tip of the cathode. The spectrometer wavelength was calibrated with a Hg-Ar spectral calibration lamp (*Oriel Instruments*, Model 6035), and in intensity with a halogen lamp (*Ocean Optics*, DH-2000). For all spectra acquired, the background radiation was recorded for the same exposure time and number of accumulations, and subtracted prior to making calibration corrections. The exposure time of the CCD array was set to 500 ms. The instrumental function of the spectrometer was obtained using a He-Ne laser.

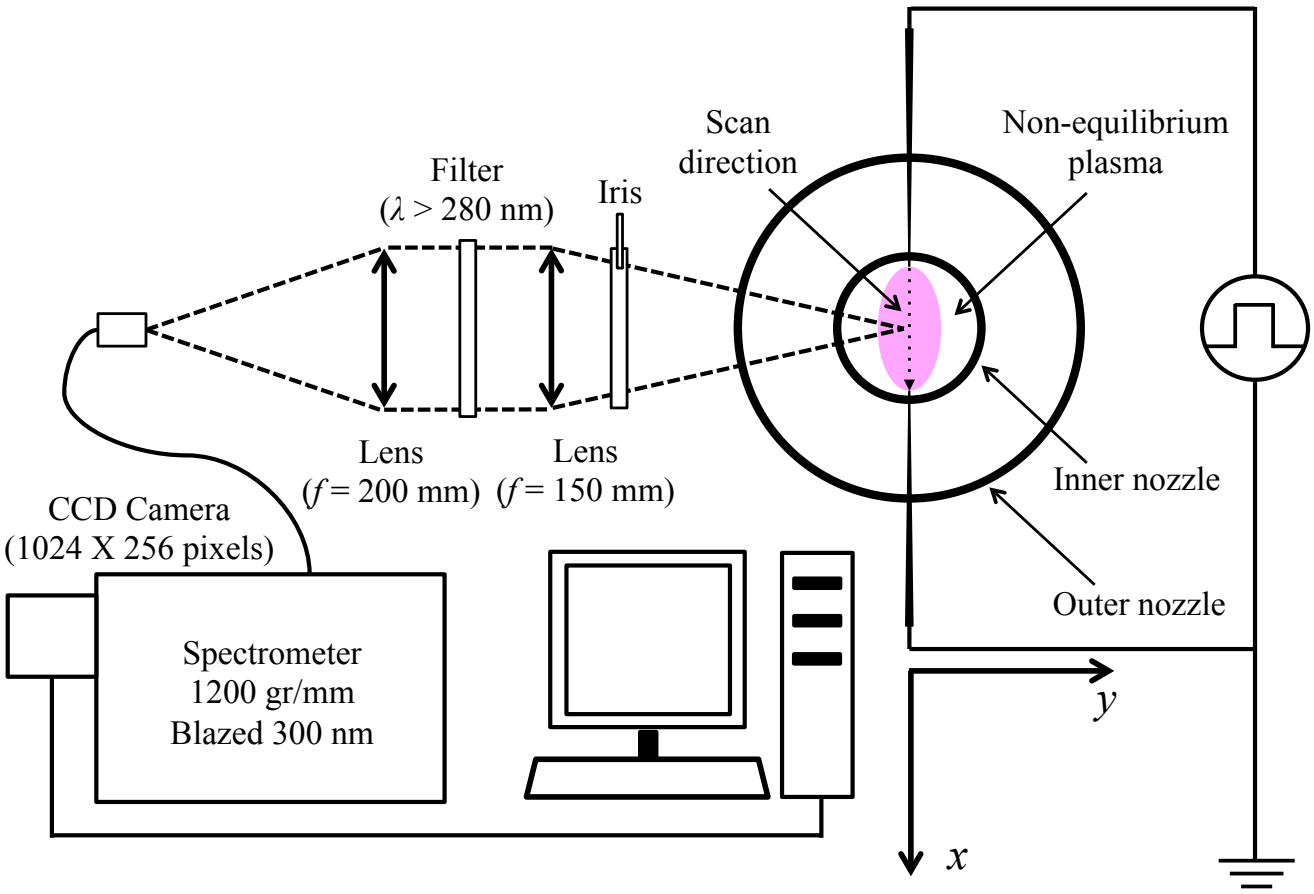

FIG. 3. Schematic of the apparatus used for optical emission spectroscopy (top view of burner).

III. RESULTS & DISCUSSION

A. Electrical Diagnostics

Figure 4 (left) shows the excitation voltage waveform used to produce the diffuse plasma. The peak voltage is 11 kV and the duration is 300 ns FWHM. Accounting for the radius of curvature of the pin electrodes,[25] the highest value of the Laplacian electric field at the tip of the anode is 10 MV/m, yielding a reduced electric field of approximately $4 \cdot 10^{-15}$

V cm^2 (400 Td). At approximately a millimeter from the anode tip, E/N decreases rapidly and remains in the 40-100 Td range, which is close to that required to obtain significant fractional energy deposition into vibrational modes and electronic states of N_2 in atmospheric pressure air.[26] The inset of Figure 4 (left) shows a digital photograph of the diffuse CH_4-air plasma in the cold flow. The plasma is visually free of constricted filaments, and the current probe detects no high-current discharges. Figure 4 (center) shows the measured current at 2 kHz, and the conduction current at 2 and 10 kHz in the cold flow. The peak value of the conduction current monotonically decreases with increasing v (~ 145 mA at 2 kHz, and ~ 70 mA at 10 kHz). Additionally, the peak conduction current value is attained faster with increasing v. This is supported by the findings of the ICCD imaging results, where the streamer travels faster with increasing v. The inset of Figure 4 (right) shows the change in the flame's position upon application of the discharge for various pulse repetition frequencies (v = 2, 4, 6 kHz). As v is increased, the flame is progressively pulled down toward the diffuse plasma. Even though the pin electrodes are positioned as accurately as possible in the center of the inner nozzle's internal diameter, the shape of the flame is somewhat distorted. The energy per pulse of the discharge, E_{pulse}, is calculated by multiplying the synchronized voltage and conduction current waveforms, and then integrating them. Figure 4 (right) shows E_{pulse} as a function of v in both the cold flow and for the downstream flame. The energy per pulse decreases with increasing v until a spark discharge is produced. This decrease with v can be attributed to the increase in propagation speed of the primary streamer, as illustrated in the streak plots of Section III.B, whereby the secondary streamer becomes a distinct event and no longer contributes to the conduction current. A further decrease in E_{pulse} with a flame can be attributed to lower N, due to some gas heating, since the energy loading per molecule is thought to be constant for diffuse nanosecond discharges.[27] It should be acknowledged that the measured decrease in coupled energy is specific to the pulse generator used, since the output pulse produces both primary and secondary streamers. If a shorter duration high-voltage pulse, producing only primary streamers, was used to produce the gas discharge, the decrease in coupled energy may not be observed. Additionally, current leakage through the flame may occur, but cannot be explicitly confirmed. The diffuse plasma exists for different frequency limits in the cold flow (2 to 10 kHz) and the downstream flame (1 to 7 kHz). Diffuse plasma is produced by applying repetitive high-voltage pulses, for a given v, until v exceeds the value required to produce a high-current spark channel. If a spark is produced, the mixture is ignited by the discharge and the flame becomes thermally anchored between the electrode pair. The earlier onset of a spark discharge when a flame is present may be explained by both the change in N as the flame approaches the plasma, and the higher electrical conductivity of the flame,[28] which can provide a preferential channel for high-current electrical breakdown. The average power deposited by the diffuse plasma ranges from 0.4 to 1.1 W in the cold flow, and from 0.3 to 0.7 W for the downstream flame; corresponding to 0.11-0.25 % of the flame's thermal power. The peak instantaneous power varies from 1.7 to 0.7 kW in the cold flow (2 to 10 kHz), and

from 2.1 to 0.9 kW in the downstream flame (1 to 7 kHz). Assuming that all the energy provided by the discharge is used to heat the mixture in the zone affected by the discharge, and not excite the gas, the temperature increase of the entire reactant flow is at most 21.4 K in the cold flow and 11.1 K in the case of a downstream flame. As will be discussed later on, such a temperature increase of the reactants is negligible with respect to the observed increase in the flame speed.

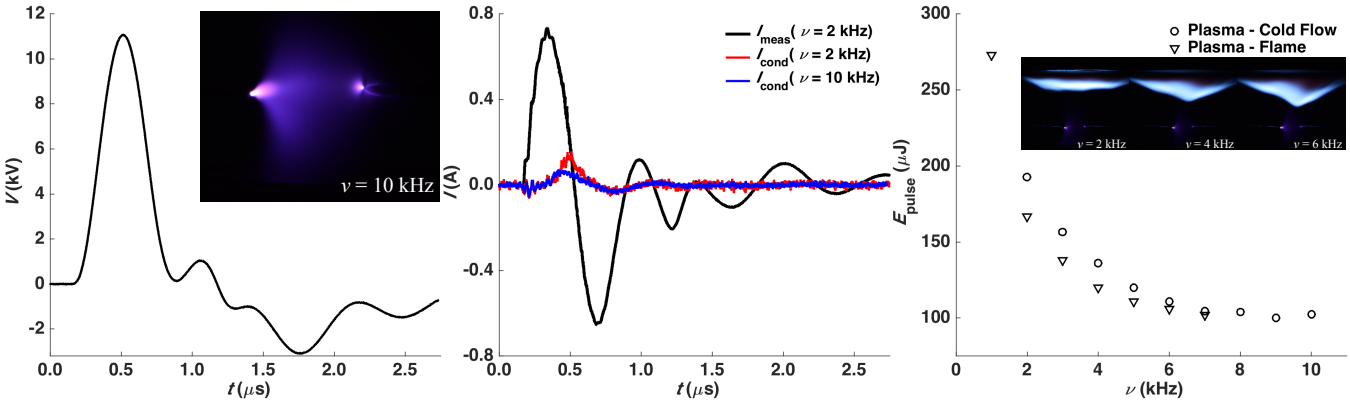

FIG. 4. Voltage waveform with digital photograph showing the diffuse discharge (left), the measured current at 2 kHz and conduction current waveforms at 2 and 10 kHz (center), and the energy coupled per pulse of the discharge with digital photographs showing the effect on a flame (right).

B. ICCD Imaging – Plasma Volume Expansion

It has been suggested that the glow-to-spark transition for high-voltage repetitively pulsed discharges at atmospheric pressure is controlled by the thermal ionization instability.[25] To further confirm this and explain the upper-frequency limits of the diffuse plasma domain observed in the previous section, time-resolved ICCD imaging was used to measure and characterize the propagation and expansion of the plasma in both the cold flow and downstream flame cases. Figure 5 shows streak plots of the plasma emission along the inter-electrode gap (x-axis) for increasing values of ν (2, 6, 10 kHz) in the cold flow. For plasma propagation dynamics a new time stamp, t_s, is used as the time from streamer inception rather than t, the reference of the trigger generator. These plots provide an overview on the type of discharge that is produced by the voltage pulse, for increasing ν. The discharge consists of a primary streamer, a secondary streamer, and confined emission events at the anode. The primary streamer is a wave, with a strong value of E/N in its head, that propagates from anode to cathode, producing the vast majority of the reactive species.[29] The secondary streamer produces emission, but propagates a limited distance from the anode (~ 2 mm), and is produced due to a persisting electric field following the primary streamer. The confined emission events are due to artifacts of the high-voltage pulse generator, which cause negligible production of excited species in the vicinity of the anode. Figure 5 shows that as ν increases the

primary streamer propagates with an increased velocity and the secondary streamer then becomes a distinct and separate event.

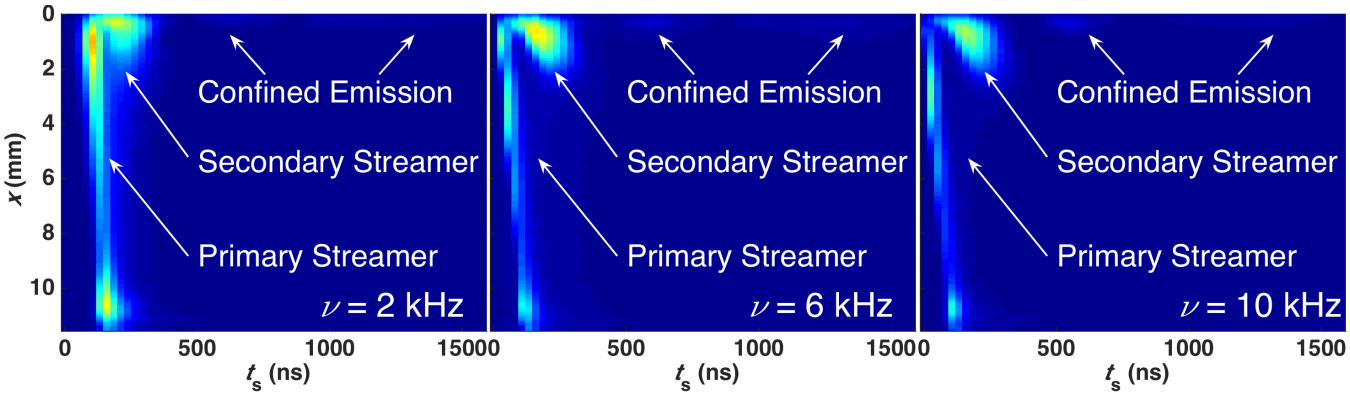

FIG. 5. Streak plots of the discharge illustrating the change in the propagation of the streamer at 2 kHz (left), 6 kHz (center), and 10 kHz (right).

Figure 6 shows ICCD images of the primary streamer propagating across the inter-electrode gap in the cold flow at a pulse repetition frequency of ν = 2 kHz. The position of the ionization front is numerically extracted, and identified on the images by the red pixels. The extent of the ionization front, along both the x-axis, χ, and the z-axis, ζ, are labeled and identified by the green and yellow pixels, respectively.

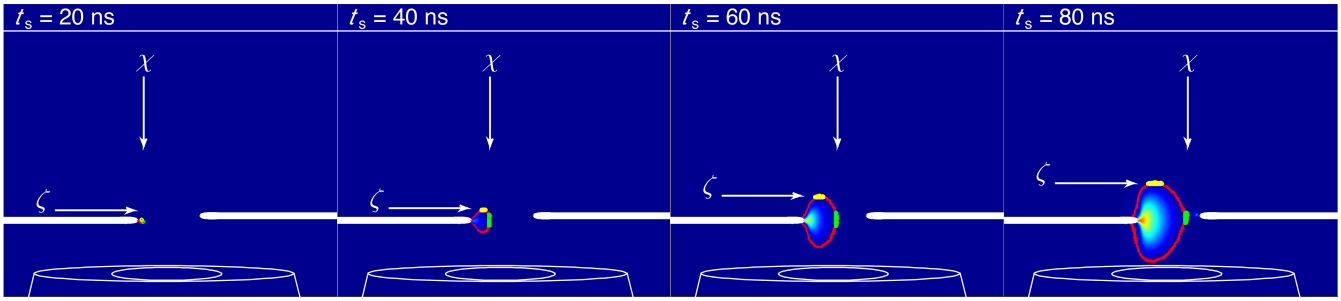

FIG. 6. ICCD images illustrating the position of the ionization front (red pixels) along the x-axis (green pixels), and along the z-axis (yellow pixels), in the cold flow at ν = 2 kHz.

Figure 7 (a, b) shows χ for the same values of t_s as in Figure 6, as a function of ν, for the case of the cold flow, and the downstream flame, respectively. As ν is increased, the ionization front travels an increasingly longer distance at a given time. This may be attributed to the accumulated species or heating from one discharge pulse to the next. Additionally, the ionization front propagates an increased distance, for the same value of ν, with a downstream flame. This may be attributed to ionization and excitation processes that occur in a larger volume of gas, on average, while the voltage at the anode still increases in time. During this increase, the local E/N in the streamer head surpasses the ionization or excitation threshold further from the anode. It should be noted that the volumetric aspect of the discharges is due to the sharpness of the

electrode tip, whereby the streamer may not necessarily start in the direction of shortest distance from anode to cathode (i.e. the anode tip). For the earlier times (t_s = 20, 40 ns), the ionization front has travelled a noticeably larger distance with increased v, a phenomenon which may be attributed to the memory effects of the discharge channel[30] and localized gas heating at the tip of the cathode, shown in the following section. For the later times (t_s = 60, 80 ns), the difference in travelled distance is less pronounced, as the ionization front has crossed the inter-electrode gap and has been halted by the cathode. The increase in χ, in the early discharge times, with the presence of a downstream flame explains the occurrence of spark transition at a lower frequency compared to the cold flow. It should be noted that the ionization front propagates further than the position of the cathode, as it expands in an ellipsoidal manner along both the x and z-axes. Figure 7 (c, d) shows ζ for the same times as in Figure 7 (a, b), as a function of v, for the case of the cold flow and the downstream flame. The ionization front propagates further downstream when a flame is present, due to the significantly lower number density caused by the temperature rise in the flame preheat zone. This observation shows that, with increasing v, excited species are transported further downstream and can be delivered to the flame front. Furthermore, the size of the plasma discharge zone produced during the propagation of the primary streamer changes with frequency and the presence of a downstream flame.

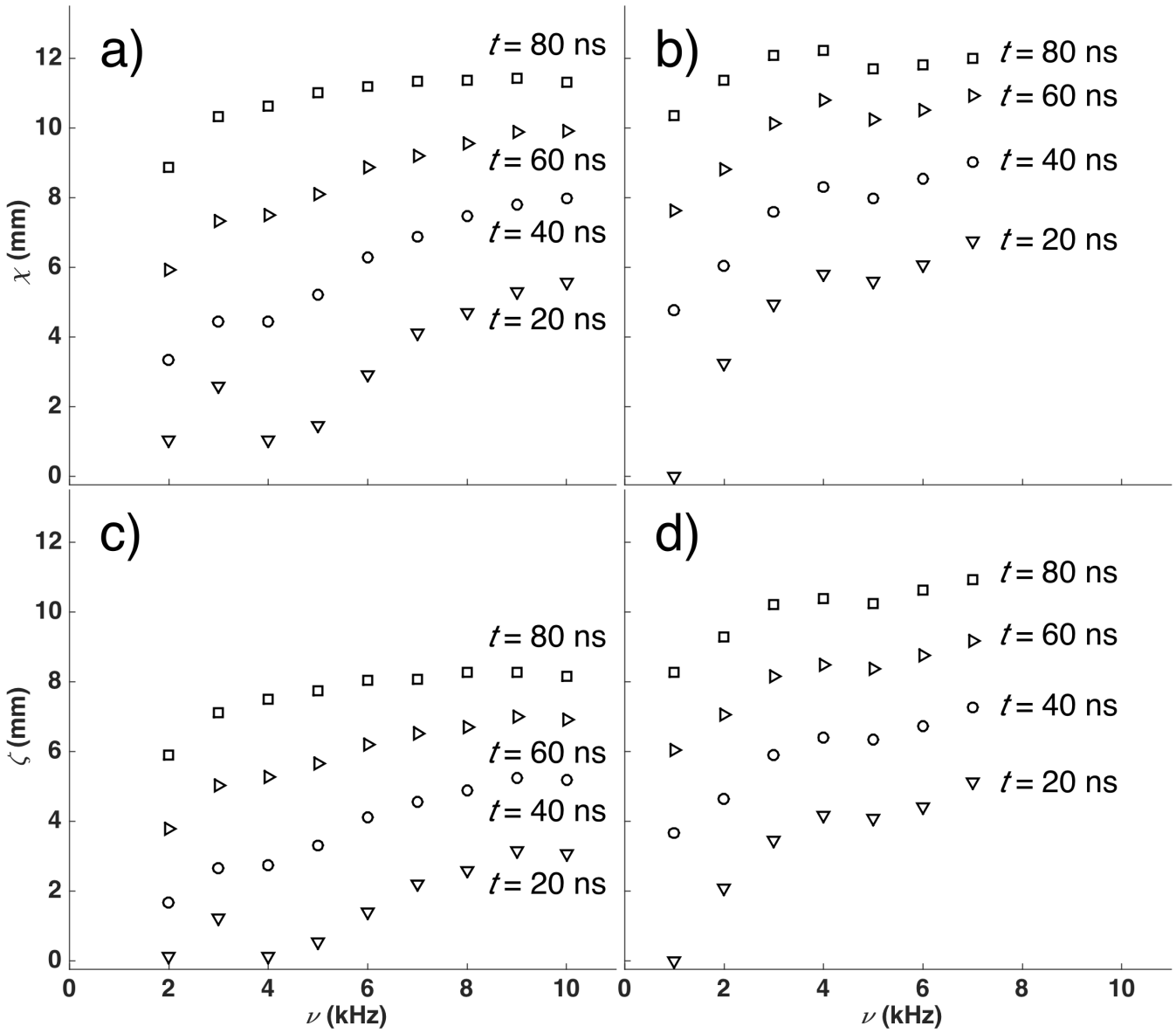

FIG. 7. χ and ζ for the various time stamps as a function of ν for the cold flow (a, c) and the downstream flame (b, d).

Since the volume of the primary streamer plasma discharge zone increases with ν and the presence of a flame, so does the residence time (τ) of the CH_4 and air molecules in the plasma discharge zone. Figure 8 (left) shows τ as a function of ν. The residence time for the cold flow increases from 18 to 25 ms (2-10 kHz), and for the downstream flame from 25 to 33 ms (1-7 kHz). The change in τ represents a significant difference in the number of pulses that are coupled to the gas molecules. Figure 8 (right) shows the number of pulses coupled to the gas during time τ as a function of ν. The number of pulses coupled to the gas ranges from 36 to 250 (2-10 kHz) in the cold flow, and of 25 to 235 pulses (1-7 kHz) for the downstream flame. Extrapolating the number of coupled pulses (N_p) to the spark transition frequency using a Hermitian polynomial, this number of pulses reaches 270 ± 3 in both cases. Since the energy per pulse prior to spark formation is

almost identical for both flow conditions (E_{pulse} ~ 100 μJ), the energy loading of the gas volume appears to control the spark transition frequency value. These data provide additional confirmation to the theory proposed by previous work,[25] and explains the lower spark transition frequency triggered by the presence of a flame, whereby the earlier onset of the thermal ionization instability is caused by a larger plasma zone and a resulting increase in τ.

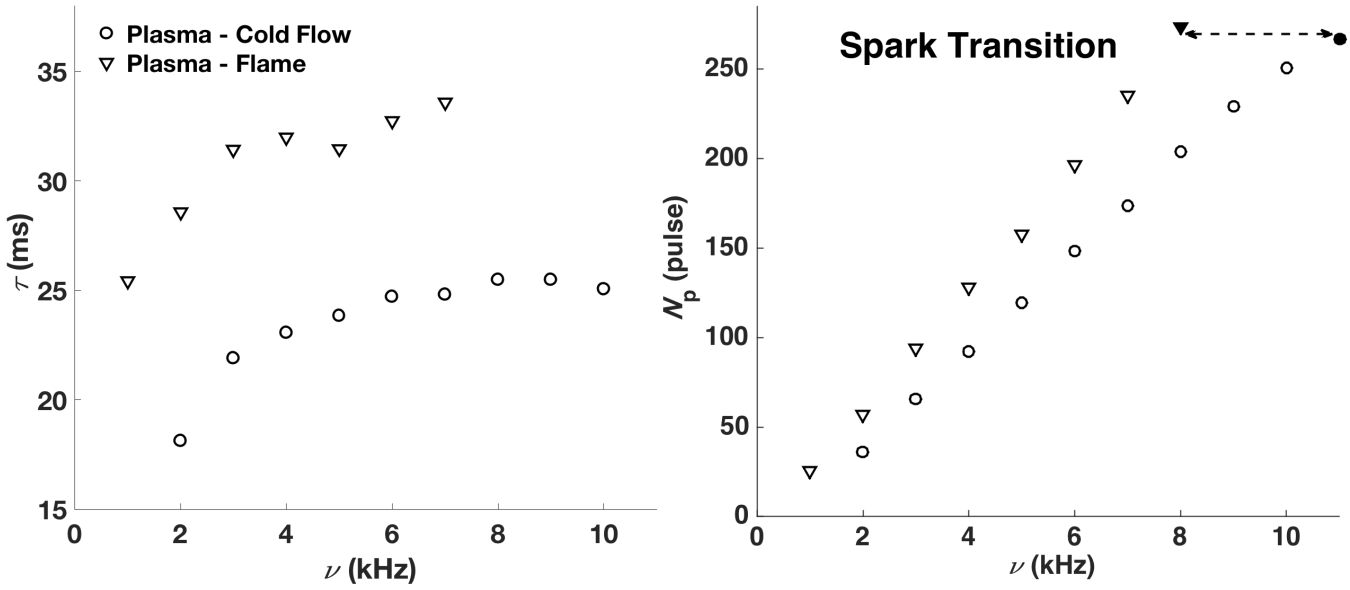

FIG. 8. Residence time of the gas in the plasma discharge zone (left), and the number of pulses coupled to the gas volume during the residence time. The black-shaded markers represent N_p extrapolated to the spark transition frequency.

C. Optical Emission Spectroscopy

Plasma can enhance the combustion process through chemical and thermal routes. In this section, the rotational temperature and the vibrational population of the $N_2(C^3\Pi_u)$ state are measured along the inter-electrode gap for all values of v, and for both flow conditions. For atmospheric pressure non-equilibrium plasmas, due to short rotational-translational relaxation times (2-3 ns), T_{rot} is a good indicator of the bulk mixture temperature,[11] and the vibrational populations are good indicators of the level of disequilibrium and chemical reactivity. The emission of fuel-lean hydrocarbon-air diffuse plasma is dominated by the second positive system of nitrogen [$N_2(C^3\Pi_u - B^3\Pi_g)$]. Figure 9 (left) shows a sample spectra collected at the tip of the cathode in the cold flow (x = 0 mm, v = 10 kHz). The spectrometer is positioned to capture several vibrational bands of the second positive system of nitrogen [$N_2(C^3\Pi_u - B^3\Pi_g)$, Δv = 1, 2, 3]. The first negative system of nitrogen [$N_2^+(B^2\Sigma_u^+ - X^2\Sigma_g^+)$, Δv = 0] can also be seen here. As time-averaged emission spectroscopy is used, the populating and depopulating mechanisms of this transient discharge are captured in these measurements. Since vibrational-

translational energy exchange is relatively slow at atmospheric pressure, the measured vibrational levels of the $N_2(C^3\Pi_u)$ state do not follow a Boltzmann distribution. Figure 9 (right) shows a plot of the relative intensity of vibrational band heads with respect to the first vibrational level of that series (v = 0) as a function of a Boltzmann vibrational temperature. As an example, the solid red line in Figure 9 (right) plots the simulated ratio of vibrational band head (1-3) to (0-2) of the $\Delta v = 2$ series as a function of the vibrational temperature. The dot placed upon this line represents the experimentally measured ratio, which is close to 3400 K. Here, the lower lying vibrational levels become more highly populated than the higher ones. As all the experimental dots do not line up along a single value of T_{vib}, a vibrational temperature cannot explicitly be characterized by a Boltzmann distribution. The experimental spectra must be described by the vibrational distribution ($f_{v'}$) rather than the Boltzmann fraction.

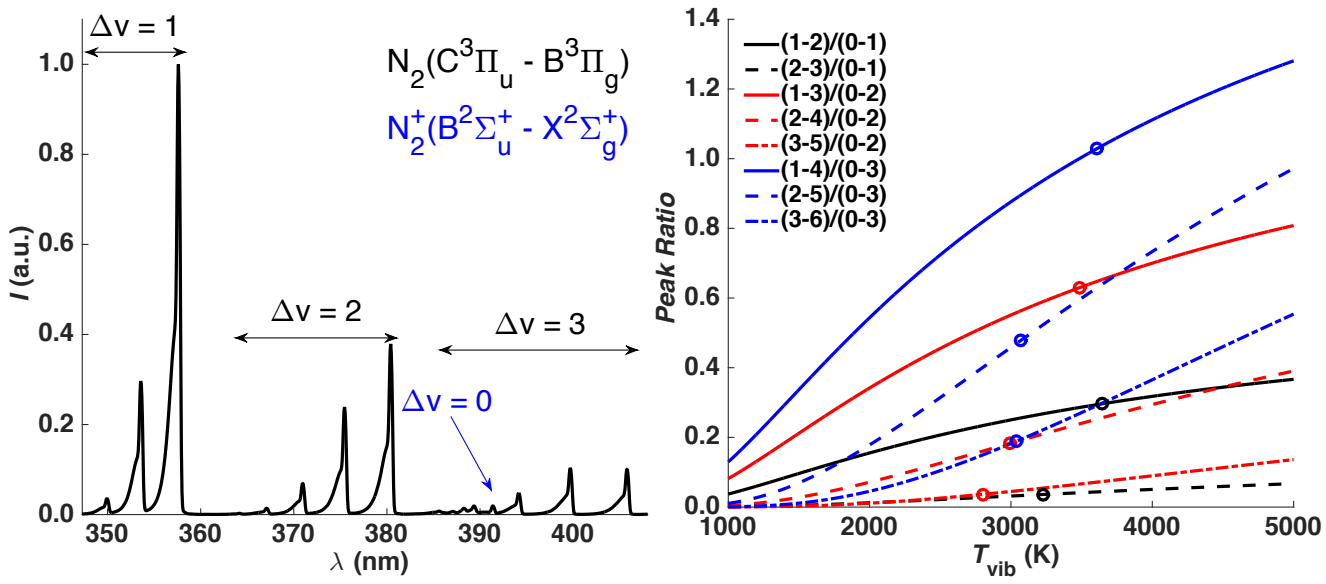

FIG. 9. Sample of the emission spectrum recorded (v = 10 kHz, x = 0 mm) in the case of the cold flow.

Equation (2) is used to simulate and fit the relative intensity of the ro-vibrational bands of the $N_2(C^3\Pi_u - B^3\Pi_g)$ system in the experimental spectra.

$$I_{\text{sim}}(\lambda) = q_{v''}^{v'}\left(R_{\text{e}v''}^{v'}\right)^2 S_{\Lambda''J''}^{\Lambda'J'}\upsilon^4 f_{v'}\exp\left(-\frac{\varepsilon_{J'}}{kT_{\text{rot}}}\right)\Phi_{\text{slit}}(\lambda-\lambda_0) \quad (2)$$

In (2), $q_{v''}^{v'}$ and $R_{\text{e}v''}^{v'}$ are the Franck-Condon factors and the electric dipole moments,[31] $S_{\Lambda''J''}^{\Lambda'J'}$ are the Hönl-London factors,[32] υ the wavenumber of the transition, and $\varepsilon_{J'}$ is the energy of the emitting rotational level. $f_{v'}$ and T_{rot} are

the vibrational distribution and rotational temperature. Φ_{slit} is the spectrometer's instrumental function, which convolves the theoretical lines and their individual intensities. No other source of line broadening is considered as the instrumental broadening is the largest.

Individual vibrational bands are fitted through the Nelder-Mead simplex algorithm to extract a mean value of T_{rot}. Fig. 10 (left) shows the result of fitting the rotational structure of six vibrational bands for the conditions of Figure 9. These vibrational bands were selected due to their high signal-to-noise ratio. The resulting mean rotational temperature for this spectrum is 413 K. Figure 10 (right) shows the result of fitting the relative vibrational distribution for each system [$N_2(C^3\Pi_u - B^3\Pi_g)$, Δv = 1, 2, 3]. The markers represent the fitted experimental vibrational population of all systems, and the curves are the Boltzmann vibrational temperature that would be associated if a vibrational temperature could be assigned. The vibrational population factors monotonically decrease from 3578 to 2875 K, illustrating the vibrational depopulating mechanisms where higher vibrational levels decay faster.[33]

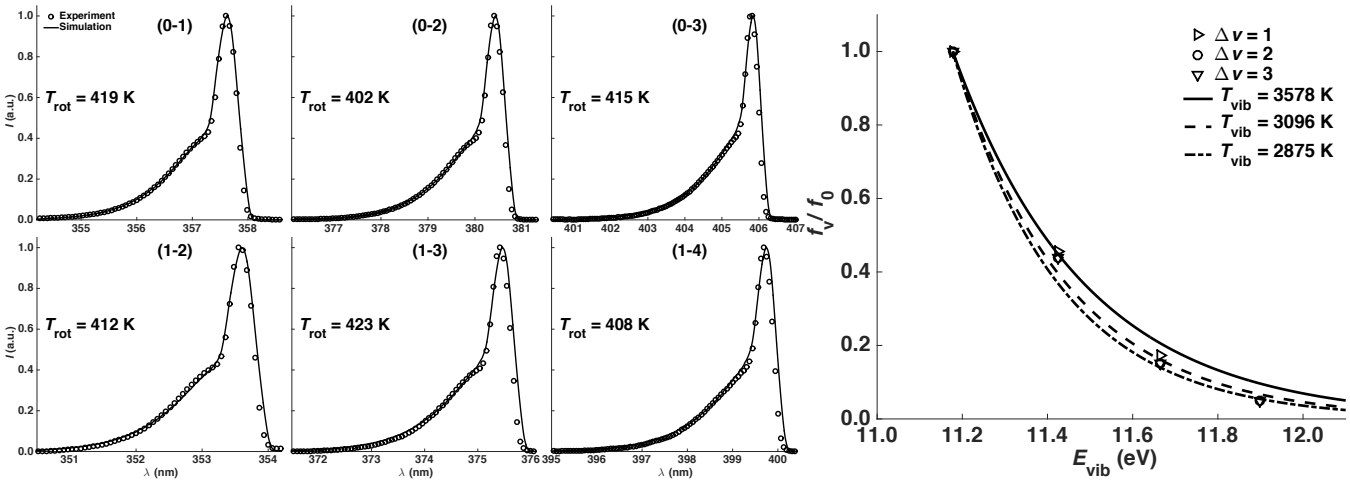

FIG. 10. Fitted individual vibrational branches to extract the rotational temperature (x = 0 mm, ν = 10 kHz).

Given the visual limitation of plotting the vibrational distribution as a function of x and v, the relative population fraction of the second vibrational level (i.e. f_1/f_0) will be used as the quantity illustrating the trend in vibrational populations. Figure 12 (a, b) shows the rotational temperature as a function of x and v, for the cold flow and downstream flame, respectively. In both cases, T_{rot} increases near the anode along the x-axis (~ 5 K/kHz) and increases with v, but remains constant around 340-360 K in the remainder of the discharge gap. The translational temperature of the gas remains relatively constant in the zone of flame stabilization with increased v. Figure 12 (c, d) shows the f_1/f_0 factor as a function of x and v. Vibrational population factor f_1/f_0 increases from anode to cathode as measured in previous work,[34] and the increase appears to be more pronounced as the pulse repetition frequency increases. Vibrational factors in the range of

0.51, corresponding to a $T_{vib} \approx 4000$ K, are reached at ν = 10 kHz in the cold flow and near the cathode. The increase of f_1/f_0 with both x and ν occurs due to the significant high-voltage drop related to the cathode sheath located near its surface.[29] From the inset of Figure 4 and the ICCD images of the flame, it can be seen that the flame stabilizes near the cathode (x = 11 mm), in the zone of highest vibrational excitation, as opposed to the zone of highest translational temperature increase near the anode (x = 0 mm).

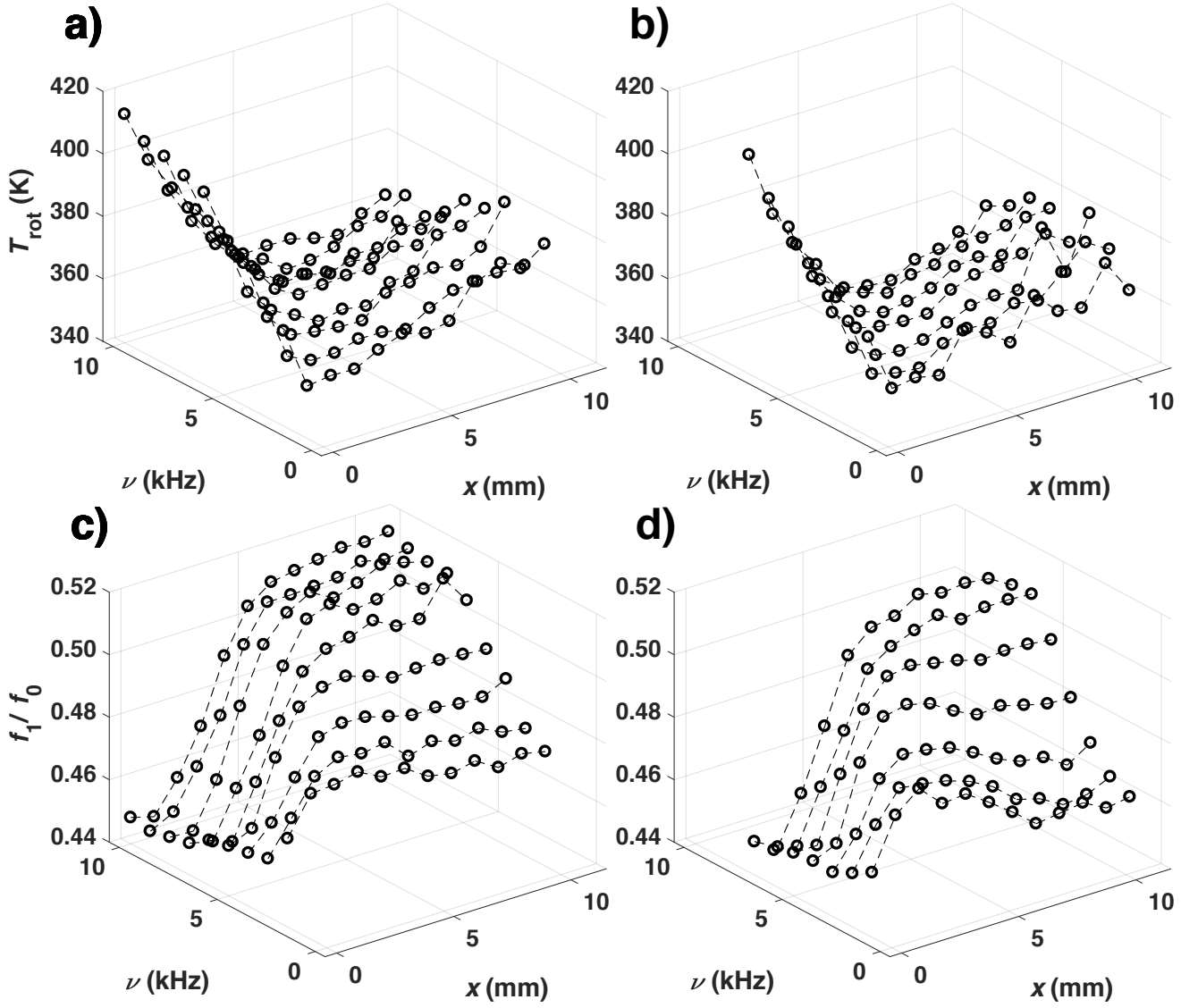

FIG. 11. Rotational temperature distribution in the anode-cathode gap (anode at x = 0 mm) for several pulse frequencies for the cold flow (a) and downstream-flame (b). Relative vibrational distribution factor f_1/f_0 for the cold flow (c), and downstream flame (d).

It should be noted that the increase in rotational temperature is localized at the tip of the anode, and along the inter-electrode gap. An increase in this quantity may be related to the production of $O_2(a^1\Delta_g)$ particles,[19] which may slightly

increase the flame speed. Flame speed simulations on Cantera using the mechanism of Li *et al.*[35] show that if the entire flow were to be heated by 60 K (the baseline increase in T_{rot} in the stabilization zone), the flame speed would increase from 0.13 to 0.18 m/s. The most important observation related to these spectroscopic measurements is that no significant increase in the rotational temperature of the $N_2(C^3\Pi_u)$ state takes place as a function of frequency, in the flame stabilization zone. The location of the stabilized flame is a good indicator of the role that the diffuse plasma may play in activating and actuating a flame at atmospheric pressure. This data present supporting evidence for the prediction of increased global reaction rates and moderately unaffected thermal diffusivity provided by vibrationally-excited species, which lead to a local increase in the flame speed S_L.[36]

D. ICCD Imaging – Flame Displacement

To investigate the response of a flame to a high-voltage pulse, the exposure time of the ICCD camera is increased (t_{exp} = 1 µs), and the delay is incrementally shifted until the next high-voltage pulse is applied in the series. Once the primary streamer has reached the cathode (t_s ~ 100 ns), the radicals produced in its head, and all subsequent phases of the discharge, are directly delivered to the flame front. Figure 12 shows the complete time-integrated discharge event ($0 \leq t \leq$ 1 µs) that couples the reactive species to the flame front for all values of v, in the steady state regime. The non-activated flame (v = 0 kHz) is located in the varying velocity field, where the flame speed matches that of the unburned CH_4-air mixture.[37] The images at lower v are brighter, as all images have the same number of on-CCD accumulations, and because E_{pulse} increases with decreasing frequency (section III. A.). Here, the emission from the plasma is directly coupled to the flame front, making use of the reactive species that are short-lived at atmospheric pressure. The leading edge of the flame (ζ_f) is defined as the most upstream location of the flame, with respect to the flow field. As v increases, the increased emission in the leading edge of the flame is more visible and the leading edge is progressively pulled closer toward the plasma discharge zone. The progression of the flame displacement produces an intimate coupling of the diffuse low-temperature plasma to the combustion zone.

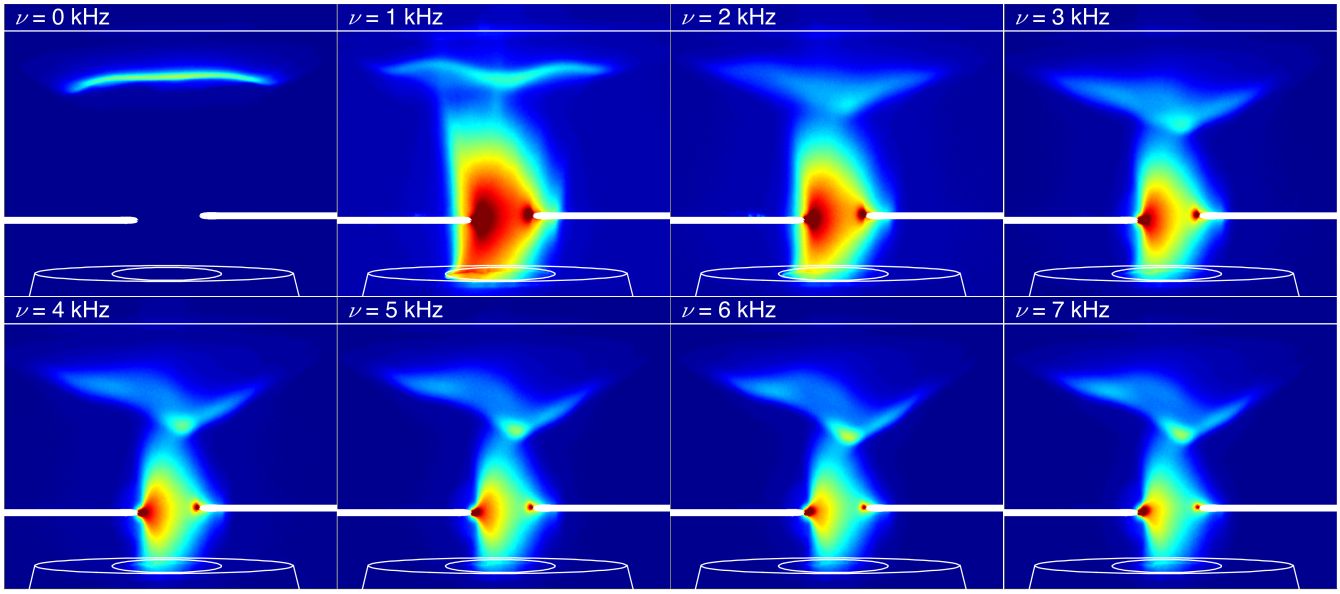

FIG. 12. ICCD images of the entire discharge event (t_{exp} = 1 μs) coupled to the flame (t = 0 μs) for various frequencies.

Following the discharge event illustrated in Figure 12, images of the flame are acquired and the location of the leading edge of the flame, ζ_f, is tracked as a function of time. Figure 13 shows results of the leading edge extraction algorithm at various times (t = 1, 50, 150 μs) following a high-voltage pulse (ν = 3 kHz). The red pixels represent the outline of the entire flame while the green pixels show the position of the leading edge of the flame. After the discharge event has passed, the short-lived UV emission disappears and ζ_f is located near the radical pool. The flame subsequently relaxes back to a certain position until the next plasma-generating pulse is applied, where ζ_f is once again pulled toward the radical pool and the cycle repeats itself.

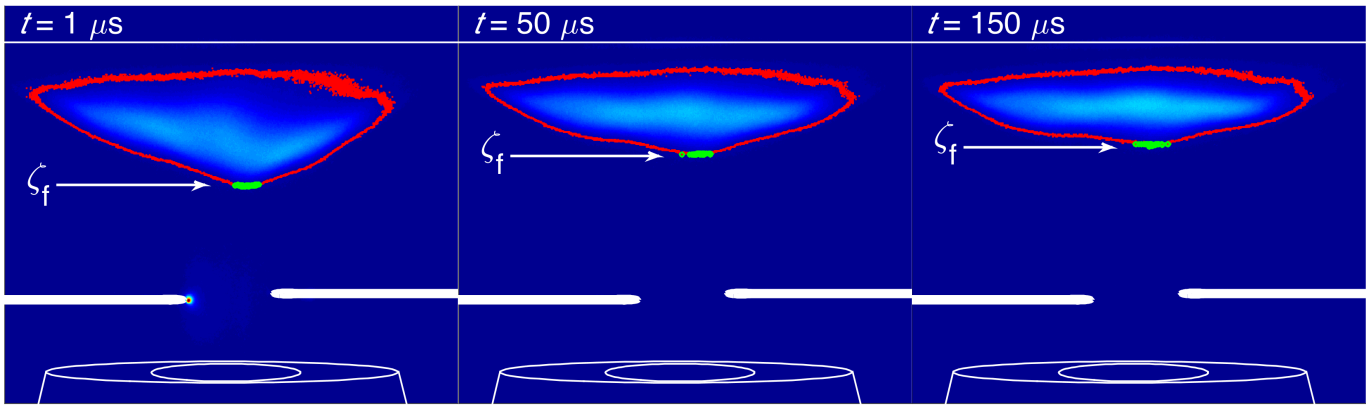

FIG. 13. ICCD images of the flame (t_{exp} = 1 μs) following a high-voltage pulse (ν = 3 kHz). The red pixels show the flame envelope and the green pixels the leading edge of the flame ζ_f.

Figure 14 shows the summary of the position of ζ_f, following a high-voltage pulse, as a function of time, for all values of ν. The value of ζ_f is adjustable and controllable with the imposed value of ν. Without plasma activation (ν = 0 kHz), ζ_f is located at the reference position (29 mm). When the discharge is operated a low ν (1 to 2 kHz), ζ_f is significantly displaced upstream (28, 24.5 mm). Pronounced dynamics are observed by further increasing ν (3 kHz), as partially illustrated in Figure 13. First, ζ_f is located near the radical pool (22 mm), and attempts to relax back to a position of equilibrium in the flow field (26 mm), prior to the application of the next high-voltage pulse. At this frequency (3 kHz), the flame appears to be oscillating in some kind of intermediate transition zone. The cause of this oscillation is repeatedly measured and still unknown. Future work will address this, specifically focusing on the range of frequencies for which these dynamics are observed. As ν further increases (5 to 7 kHz), the flame is displaced further upstream into the unburned mixture, but with a diminished shift in the location of ζ_f with ν, when compared to lower pulse repetition frequencies (1 to 4 kHz).

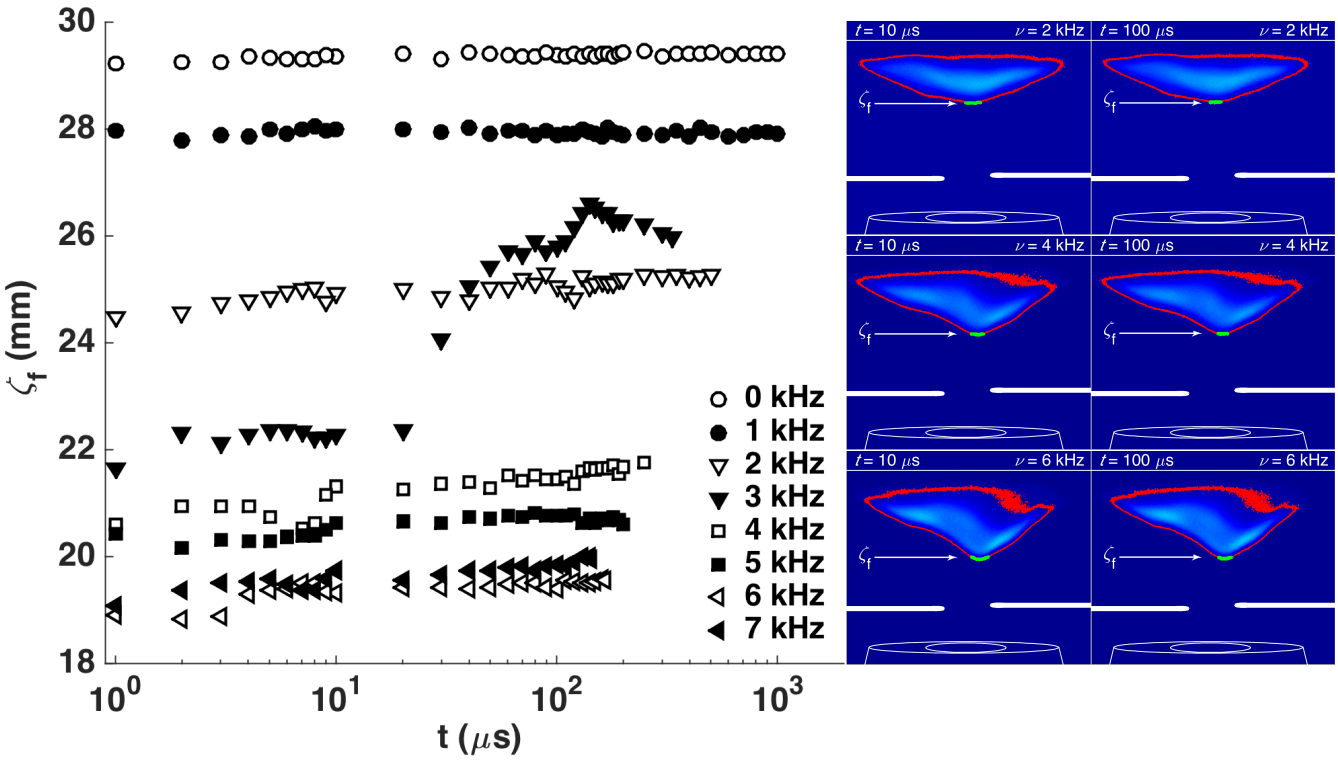

FIG. 14. Flame-root location as a function of time, for all values of ν (left), and sample ICCD images of the flame for selected frequencies (ν = 2, 4, 6 kHz), at two times (t = 10, 100 µs) following a discharge pulse (right).

Since little-to-no increase in the rotational temperature was observed as a function of ν in the flame stabilization zone, this might suggest that the upstream velocity profile could be unaffected by a thermal mechanism. On the other hand,

strong hydrodynamic contributions of the discharge have been observed following a high-current nanosecond-duration spark (~ 10 ns),[38] yielding a toroid-like pressure wave.[39] Since the discharge produced here is not a spark filament, and the energy is deposited over a significantly longer period of time (~ 300 ns), hydrodynamic contributions may not be major contributors to flow field distortions. Therefore, if flow perturbations induced by the discharge appear to be relatively weak, a shift in the position of the leading edge of the flame indicates strong evidence for the increase in the reactivity of the flame through the addition of a low-temperature radical pool. This would imply an increase in the oxidation rates of hydrocarbons through the addition of minute quantities of atomic and metastable oxygen, or fragmented fuel molecules. These results show strong evidence of chemical activation and actuation of a flame's dynamics, at atmospheric pressure, by diffuse non-equilibrium plasma. In future work, Schielren imaging should be used to investigate the hydrodynamic perturbation provided by a repetitively-pulsed diffuse discharge to this flow field.

IV. Conclusion

Diffuse non-equilibrium plasma was used to activate a lean-premixed CH_4-air stagnation flame. ICCD imaging and electrical diagnostics were used to explore and explain the limits of diffuse plasma for the case of the cold flow and downstream flame. The energy deposited per pulse of the discharge decreased monotonically with v, and reached approximately 100 μJ prior to spark channel formation, for both the cold flow and downstream flame. ICCD imaging revealed that the primary streamer travelled faster, and expanded further downstream, with increased v and with the presence of a downstream flame. This explained the decrease in the upper frequency limit of the diffuse regime brought on by the thermal ionization instability resulting from the direct coupling of the flame pre-heat zone to the discharge. OES measurements showed that the rotational temperature of the $N_2(C^3\Pi_u)$ state slightly increases with v near the anode surface, but remains relatively constant throughout the discharge gap and in the flame stabilization zone (T_{rot} = 340-360 K). OES measurements also revealed that relatively high non-equilibrium vibrational populations, which are a good indicator of increased chemical reactivity, are produced near the cathode where the flame stabilizes. ICCD imaging of the flame shows that the leading edge of the flame can be displaced upon controlling v. These results provide evidence that low-temperature diffuse plasma can be used to chemically activate and control a stabilized CH_4-air flame at atmospheric pressure.

V. Acknowledgements

M.D.G. Evans would like to acknowledge the financial support of the McGill Engineering Doctoral Award through the Tomlinson award, as well as the *Fonds de Recherche Québec Nature et Technologies* through the B2 award.

The authors would like to thank the financial support of the Natural Sciences and Engineering Research Council of Canada, the Gerald Hatch Faculty Fellowship, and Siemens Canada.

VI. References

[1] Y. Ju and W. Sun, Prog. Energy Combust. Sci. **48**, 21 (2015).

[2] S.M. Starikovskaia, J. Phys. D. Appl. Phys. **47**, 353001 (2014).

[3] A.Y. Starikovskii, N.B. Anikin, I.N. Kosarev, E.I. Mintoussov, S.M. Starikovskaia, and V.P. Zhukov, Pure Appl. Chem. **78**, 1265 (2006).

[4] V.Y. Basevich and A.A. Belyaev, Sov. J. Chem. Phys. **9**, 1874 (1992).

[5] Z. Yin, K. Takashima, and I.V. Adamovich, IEEE Trans. Plasma Sci. **39**, 3269 (2011).

[6] D.R. Singleton, A. Kuthi, J.M. Sanders, M.A. Gundersen, A. Simone, and S.J. Pendleton, IEEE Trans. Dielectr. Electr. Insul. **18**, 1084 (2011).

[7] J.K. Lefkowitz and T. Ombrello, Combust. Flame **180**, 136 (2017).

[8] M. Pinchak, T. Ombrello, E. Gutmark, V. Katta, and T. Ombrello, Philos. Trans. R. Soc. A Math. Phys. Eng. Sci. **373**, 17 (2015).

[9] I.V. Adamovich, W.R. Lempert, J.W. Rich, Y.G. Utkin, and M. Nishihara, J. Propuls. Power **24**, 1198 (2008).

[10] D.A. Lacoste, J.P. Moeck, D. Durox, C.O. Laux, and T. Schuller, Vol. 1A Combust. Fuels Emiss. **135**, 1 (2013).

[11] D.L. Rusterholtz, D.A. Lacoste, G.D. Stancu, D.Z. Pai, and C.O. Laux, J. Phys. D. Appl. Phys. **46**, 464010 (2013).

[12] D.Z. Pai, D.A. Lacoste, and C.O. Laux, Plasma Sources Sci. Technol. **19**, 65015 (2010).

[13] G.L. Pilla, D.A. Lacoste, D. Veynante, and C.O. Laux, IEEE Trans. Plasma Sci. **36**, 940 (2008).

[14] S. Barbosa, G. Pilla, D.A. Lacoste, P. Scouflaire, S. Ducruix, C.O. Laux, and D. Veynante, Philos. Trans. R. Soc. A Math. Phys. Eng. Sci. **373**, 20140335 (2015).

[15] D.A. Lacoste, J.P. Moeck, C.O. Paschereit, and C.O. Laux, J. Propuls. Power **29**, 748 (2013).

[16] A.M. Starik, V.E. Kozlov, and N.S. Titova, Combust. Flame **157**, 313 (2010).

[17] T. Ombrello, S.H. Won, Y. Ju, and S. Williams, Combust. Flame **157**, 1916 (2010).

[18] T. Ombrello, S.H. Won, Y. Ju, and S. Williams, Combust. Flame **157**, 1906 (2010).

[19] A.M. Starik, P.S. Kuleshov, A.S. Sharipov, V.A. Strelnikova, and N.S. Titova, Proc. Combust. Inst. **34**, 3277 (2013).

[20] N.A. Popov, Plasma Sources Sci. Technol. **25**, 43002 (2016).

[21] C. Guerra-Garcia, M. Martinez-Sanchez, R.B. Miles, and A. Starikovskiy, Plasma Sources Sci. Technol. **24**, 55010 (2015).

[22] M.D.G. Evans, J.M. Bergthorson, and S. Coulombe, IEEE Trans. Plasma Sci. **44**, 2429 (2016).

[23] D.A. Lacoste, J.P. Moeck, W.L. Roberts, S.H. Chung, and M.S. Cha, Proc. Combust. Inst. **36**, 1 (2015).

[24] D.A. Lacoste, Y. Xiong, J.P. Moeck, S.H. Chung, W.L. Roberts, and M.S. Cha, Proc. Combust. Inst. **36**, 1 (2016).

[25] D.Z. Pai, D.A. Lacoste, and C.O. Laux, J. Appl. Phys. **107**, 93303 (2010).

[26] N.L. Aleksandrov, F.I. Vysikailo, R.S. Islamov, I.V. Kochetov, A.P. Napartovich, and V.G. Pevgov, High Temp. (Teplofizika Vysok. Temp. **19**, 17 (1981).

[27] I.V. Adamovich, M. Nishihara, I. Choi, M. Uddi, and W.R. Lempert, Phys. Plasmas **16**, 113505 (2009).

[28] G. Colonna, L.D. Pietanza, A. D'Angola, A. Laricchiuta, and A. Di Vita, Plasma Sources Sci. Technol. **26**, 25008 (2017).

[29] S. V Pancheshny, S.V. Sobakin, S.M. Starikovskaya, and A.Y. Starikovskii, Plasma Phys. Reports **26**, 1054 (2000).

[30] S. Nijdam, E. Takahashi, A.H. Markosyan, and U. Ebert, Plasma Sources Sci. Technol. **23**, 25008 (2014).

[31] F.R. Gilmore, R.R. Laher, and P.J. Espy, *Franck-Condon Factors, R-Centroids, Electronic Transition Moments, and Einstein Coefficients for Many Nitrogen and Oxygen Band Systems* (Alexandria, VA, 1992).

[32] G. Herzberg, *Molecular Spectra and Molecular Structure - Vol I. Spectra of Diatomic Molecules*, Second (D. Van Nostrand Company, LTD, London, 1939).

[33] S.V. Pancheshnyi, S.M. Starikovskaia, and A.Y. Starikovskii, Chem. Phys. **262**, 349 (2000).

[34] M.D.G. Evans, F.P. Sainct, F. Aristizabal, J.M. Bergthorson, and S. Coulombe, J. Phys. D. Appl. Phys. **48**, 255203 (2015).

[35] J. Li, Z. Zhao, A. Kazakov, M. Chaos, F.L. Dryer, and J.J. Scire, Int. J. Chem. Kinet. **39**, 109 (2007).

[36] H.C. Jaggers and A. von Engel, Combust. Flame **16**, 275 (1971).

[37] J.M. Bergthorson, S.D. Salusbury, and P.E. Dimotakis, J. Fluid Mech. **681**, 340 (2011).

[38] D. Xu, M.N. Shneider, D.A. Lacoste, and C.O. Laux, J. Phys. D. Appl. Phys. **47**, 235202 (2014).

[39] S. Stepanyan, J. Hayashi, A. Salmon, G.D. Stancu, and C.O. Laux, Plasma Sources Sci. Technol. **26**, 1 (2017).